

# Measuring the evolution of early-type galaxies in GAMA using observationally robust quantities

Rongfu Liu, Alessandro Sonnenfeld

Accepted XXX. Received YYY; in original form ZZZ

## ABSTRACT

This is a simple template for authors to write new MNRAS papers. The abstract should briefly describe the aims, methods, and main results of the paper. It should be a single paragraph not more than 250 words (200 words for Letters). No references should appear in the abstract.

**Key words:** keyword1 – keyword2 – keyword3

## 1 INTRODUCTION

Early type galaxies (ETGs), which are typically elliptical in shape, are believed to be passively evolved after their star-forming activities being quenched. Over the past few decades, observations have confirmed that the ETGs at the epoch of  $z \approx 2$  are much more compact than their counterpart at  $z \approx 0$  (Daddi et al. (2005), Toft et al. (2007), Trujillo et al. (2006), Trujillo et al. (2007), van Dokkum et al. (2008)). These ultra-compact objects then experienced a dramatic growth in size, in particular, by about a factor of 3 between  $z = 2$  and  $z = 0$  (Damjanov et al. (2019); Fan et al. (2008); Hamadouche et al. (2022); van der Wel et al. (2014); van Dokkum et al. (2010)). Numerous works in literature have confirmed that the dissipationless dry mergers is the major mechanism that attribute to that rapid size growth. (e.g. Naab et al. (2009), van Dokkum & Brammer (2010), Oser et al. (2011), Newman et al. (2012), Hilz et al. (2013), Dekel & Burkert (2014), D'Eugenio et al. (2023)), especially for mergers with mass ratio around 1:10 (Newman et al. (2012); Belli et al. (2015)). However, purely minor merger is not sufficient to explain the entire growth, or the number of mergers will be too large in that case (Hopkins et al. (2010); Nipoti et al. (2009)) while the constrain placed by the density slope of galaxies cannot be satisfied (Sonnenfeld et al. (2014)). Some other mechanisms or observational effects must be taken into consideration, such as dry mergers with higher mass ratio (major merger) and the existence of the color gradient.

At relatively lower redshift, newly quenched galaxies may join the population of quiescent galaxies. These "fresh blood" of quiescent population are relatively larger, thus could mimic the growth in size of such galaxies. This effect is called "progenitor bias" (Dokkum & Franx (1996); Carollo et al. (2013); Fagioli et al. (2016); van Dokkum & Franx (2001)), and it is also an important effect that may contribute to the observed size evolution of ETGs. Each of these effect will leave impact on some other observable properties of galaxy, such as velocity dispersion, number density and mass, while these impact could in turn place constrains on the effects above. Nevertheless, a theoretical model that could meet all these constrains is still in absence.

Besides, another systematic might be ignored in the literature. The problem arise from the finite photometric depth of observations. it is hard to measure the total light directly (Tal & van Dokkum (2011)) as

the information where the surface brightness of galaxies drops below the observation limit remains unknown. To obtain a accurate measurement of the total light, a precise sky-subtraction is demanded while it is easy to bring additional systematic. In literature, we use various models to fit the surface brightness distribution of galaxies. The faint outskirt of galaxies could not provide reliable constrains during the fitting process, thus the model could not be able to provide reliable descriptions for surface brightness there. These unreliable data will be accounted in the total light measurement and will take up an ineligible fraction (up to 20% according to Sonnenfeld (2020)). However, the traditional definition of galaxy size and mass derived from the best-fit model are both associated with the total light, therefore we believe they are not robust qualities.

Instead of investigating the whole galaxy, we may focus on a fixed, relatively small aperture and investigate some properties inside, following the method proposed in Sonnenfeld (2020). In this work, we choose 10kpc as that aperture, in consideration that it is large enough to enclose sufficient amount of stellar mass while will not be too large to suffer from the extrapolation problem. We use  $M_{*,10}$  to denote the mass enclosed inside 10kpc and  $\Gamma_{*,10}$  to represent to mass-weighted projected surface density slope. The latter is defined as

$$\Gamma_{*,10} = \frac{2\pi \int_0^{10} R \frac{d\log \Sigma_*}{d\log R} \Sigma_*(R) dR}{2\pi \int_0^{10} R \Sigma_*(R) dR} = 2 - \frac{2\pi \times 10^2 \times \Sigma_*(10)}{M_{*,10}} \quad (1)$$

Assuming a isothermal density profile for elliptical galaxy, the growth in total stellar mass and effective radius due to mergers can be approximated using virial theorem (Naab et al. 2009). In particular, if the mass of one galaxy grow by a factor of  $\eta$ , i.e.  $M_f = (1+\eta)M_i$ , then the growth of gravitational radius can be expressed as  $r_f = \frac{(1+\eta)^2}{(1+\eta)\epsilon} r_i$ , here  $\epsilon$  is the ratio of mean square velocity of the accreted galaxy to that of the progenitor galaxy. However, switching to  $M_{*,10}$  and  $\Gamma_{*,10}$  space, it's hard to derive a relation in  $\Delta M_{*,10}$  and  $\Delta \Gamma_{*,10}$  analytically as a fixed aperture size 10kpc is involved. Nevertheless, N-body simulations can be helpful. We utilize the simulation result from Nipoti et al. (2009) which contains a number of binary mergers with different mass ratio. We measure the  $M_{*,10}$  and  $\Gamma_{*,10}$  of both progenitor and merger remnant and calculate the growth in these two quantities. In addition to finding that different merger ratio

behaves differently, we also discovered that the scale of galaxy also make differences.

Having find how the  $M_{*,10}$  and  $\Gamma_{*,10}$  under different growth scenarios, we then compared them with the evolution of these two quantities in reality. We select ETGs from GAMA DR4 main survey (Galaxy and Mass Assembly, [Driver et al. \(2022\)](#); [Bellstedt et al. \(2020\)](#); [Baldry et al. \(2010\)](#); [Hopkins et al. \(2013\)](#)) and obtained precise spectroscopic redshift and other quantities that related to spectrum measurement, e.g. stellar mass. In addition, the structural parameter are measured from KiDs photometry (Kile Degree survey, [Kuijken et al. \(2019\)](#), [Roy et al. \(2018\)](#), [Amaro et al. \(2021\)](#)) using GalNet ([Li et al. \(2022\)](#)). Based on these observation datas, we then calculated their  $M_{*,10}$  and  $\Gamma_{*,10}$  and further analyse the  $M_{*,10} - \Gamma_{*,10}$  relation and their evolution from  $z = 0.6$  to present.

The structure of this paper is as follows. In Sect.2, we give a brief description on both observations from KiDs&GAMA and the binary merger simulation from ([Nipoti et al. 2009](#)). I present the result of growth of  $M_{*,10}$  and  $M_{*,10} - \Gamma_{*,10}$  in different merger scenarios in Sect.3 and present the comparison with observation result in Sect.4. Finally, I give a discussion in Sect.5 then conclude the paper in Sect.6.

In this paper, we assume a flat  $\Lambda$ CDM cosmology with  $\Omega_M = 0.3$  and  $H_0 = 70 \text{ km s}^{-1} \text{ Mpc}^{-1}$ . Magnitude are in AB units and stellar mass are in solar units.

## 2 DATA

### 2.1 observation sample selection

In this work, we need precise redshift measurment to ensure the stellar mass and aperture size of 10  $kpc$  is accurate. Therefore, we choose to use more reliable spectroscopic redshift instead of photometric redshift, obtaining measurement from ETGs in GAMA DR4. In practice, I use DMU gkvScienceCatv02([Bellstedt et al. \(2020\)](#)) to select galaxies from GAMA DR4 Main Survey sample, which only include galaxies whose r-band magnitude is larger than 19.65 in order to ensure the 95% spec-z completeness of the sample. Further, I obtain the intensity of emission lines from DMU GaussFitSimplev05 (see [Gordon et al. \(2017\)](#)) and obtain the stellar mass measurement from DMU StellarMassesGKVv24( see [Driver et al. \(2022\)](#)). According to [Taylor et al. \(2011\)](#), estimation of stellar mass was done by fitting the [Bruzual & Charlot \(2003\)](#) stellar evolution models with [Chabrier \(2003\)](#) stellar initial mass function (IMF) and the [Calzetti et al. \(2000\)](#) dust curve . In particular, the SEDs was weighted to ensure the model-fitting was operated within a fixed wavelength range (3000 - 11000Å).

In order to select ETGs, we applied a cut on  $H\beta$  equivalent width:  $Ew_{H\beta} < 0$ , to exclude galaxies with star-forming activities. In addition, I removed galaxies whose normalized redshift quality  $nQ < 2$  following the suggestion by GAMA Collaboration([Driver et al. \(2022\)](#)).

In addition, we exclude galaxies that are not overlapped with KiDs([Kuijken et al. \(2019\)](#)), in order to utilize the measurement of structural parameters. The structural parameter are measured by GalNet([Li et al. \(2022\)](#)), which has operated a single Sérsic model fitting to the surface brightness of KiDs DR5 galaxies(RUILI IN PREPARATION) using its r-band photometry. I further exclude some galaxies with catastrophic measurement which gives ridiculous values of effective radius or stellar mass. Eventually we have 79672 ETGs with measurement of spectroscopic redshift, stellar mass and structural parameters.

### 2.2 Structural parameter

As is mentioned above, the reason that we do not trust  $M_*$  (total stellar mass) and  $R_e$  (effective radius) in traditional structural parameters is the fact that they are related with the unreliable data in the outer region of a galaxies which can only be obtained by extrapolate the surface brightness model. However, we believe that best-fitting model is well-constrained by the inner region, and thus it is reasonable to use them describing shape of the surface brightness profile there. In particular, we utilize these structural parameters to calculate  $M_{*,10}$  and  $\Gamma_{*,10}$ , the procedure of which is described in Sect.2.2.2.

#### 2.2.1 Surface brightness model

In our fitting, we use Sérsic profile to model the surface brightness of galaxies :

$$I(R) = I_0 \exp \left\{ -b_n \left( \frac{R}{R_e} \right)^{1/n} \right\} \quad (2)$$

Here,  $q$  is the axis ratio,  $n$  is the Sérsic index while  $R$  is the circularised radius

$$R^2 = qx^2 + \frac{y^2}{q} \quad (3)$$

where  $x, y$  are Cartesian coordinates, located at the center of galaxies. We use symbol  $x$  to denote the axis that is aligned with the semi-major axis of the ellipse, while using  $y$  to denote axis aligned with semi-minor axis. The effective radius  $R_e$  is circularised as well.

Integrating Eq.2, we can obtain the light enclosed in a certain aperture  $L(< R)$  (or the total light  $L_{tot}$ )

$$L(< R) = 2\pi n \cdot I_0 R_e^2 \cdot \frac{1}{(b_n)^{2n}} \cdot \gamma \left[ 2n, b_n \left( \frac{R}{R_e} \right)^{\frac{1}{n}} \right] \quad (4)$$

$$L_{tot} = 2\pi n \cdot I_0 R_e^2 \cdot \frac{1}{(b_n)^{2n}} \cdot \Gamma(2n) \quad (5)$$

Here  $\Gamma$  is the gamma function,  $\gamma$  is the lower incomplete gamma function and  $b_n$  is a constant that ensure the light enclosed within the effective radius  $R_e$  is a half of the total light.

$$L_{tot} = 2L(< R_e) \quad (6)$$

Therefore,  $b_n$  can be calculated by solving

$$\Gamma(2n) = 2\gamma(2n, b_n) \quad (7)$$

In fact, galaxies may have various component, hence single Sérsic model might not be able to give a accurate description of the entire surface brightness profile. However, as we are focusing on the inner region of the galaxy, our only requirement is just the surface brightness in the inner region of galaxy can be accurately described by model. Therefore, we compared the profile of the enclosed light of galaxies with their best-fitting Sérsic model in Fig 1 . We can easily observe that although some model do have discrepancy at some large radii, the enclosed light within 10  $kpc$  is still well constrained by model.

#### 2.2.2 $M_{*,10}, \Gamma_{*,10}$ Calculation

In our work, we assume that there is no mass-to-light ratio gradient inside one galaxy, hence the mass profile can be easily obtained via the light profile. We have obtained the stellar mass estimate for each galaxy from GAMA together with the light they use in the SPS

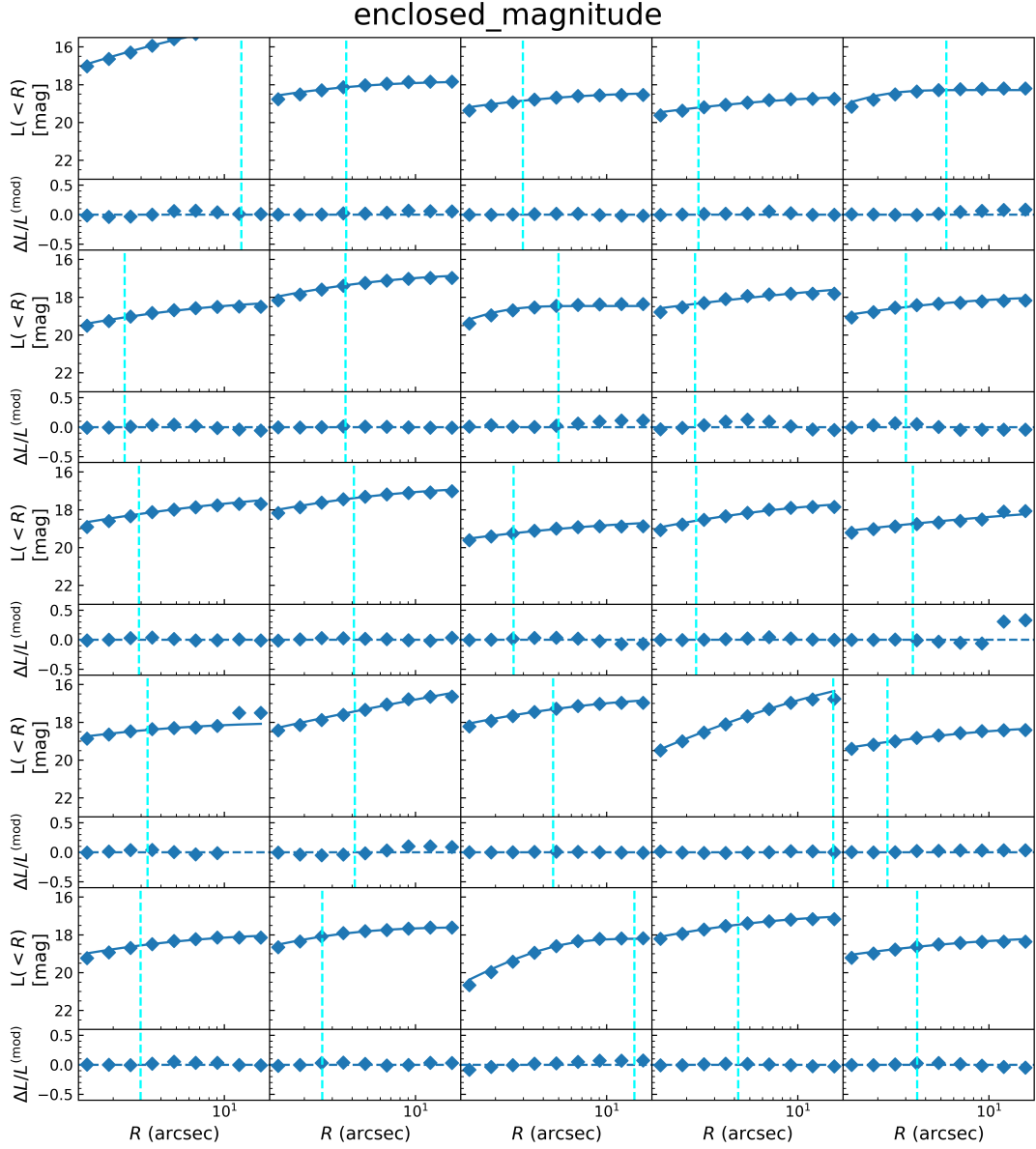


**Figure 1.** The upper panel shows the enclosed magnitude within 10kpc aperture of 25 galaxies that are random selected from our sample. The blue solid line shows the best-fitting Sérsic model calculated using GalNet structural parameters, while the blue diamonds are directly measured from KiDs r-band image. The lower panel shows the difference between the two measurements. The vertical dashed cyan line shows the corresponding angular size of 10kpc of each galaxy.

model fitting process (Driver et al. 2022), which enable us to calculate the mass-to-light ratio  $\Upsilon$ . The mass profile can be easily obtained by multiplying Eq3 and Eq4 with that  $\Upsilon$ .

$$\Sigma_*(R) = \Upsilon I_0 \exp \left\{ -b_n \left( \frac{R}{R_e} \right)^{1/n} \right\} \quad (8)$$

$$M_*( < R ) = \Upsilon 2\pi n \cdot I_0 R_e^2 \cdot \frac{1}{(b_n)^{2n}} \cdot \gamma \left[ 2n, b_n \left( \frac{R}{R_e} \right)^{\frac{1}{n}} \right] \quad (9)$$

Simply substitute  $R = 10\text{kpc}$  to Eq9, we obtained  $M_{*,10}$ , while  $\Gamma_{*,10}$  is obtained by substituting Eq8 to Eq1.

### 2.3 Completeness

To accurately measure the evolution of  $M_{*,10}$  and  $M_{*,10} - \Gamma_{*,10}$  relation, we do not expect any bias be introduced during the sample selection procedure. Therefore, we need our sample to be complete in  $M_{*,10}$ . Our fiducial sample is flux-limited, with its 95% completeness limit down to r-band magnitude 19.65. To obtain a  $M_{*,10}$  complete sample, we need to translate this completeness limit in magnitude to limit in  $M_{*,10}$ .

Then we need to translate the r-band critical magnitude  $r_{crit} = 19.65$  to one critical  $M_{*,10}$ , namely  $M_{*,10}^{crit}$ . In fact, at arbitrary redshift, the ratio between  $M_{*,10}$  and the total flux  $F$  always spread a relatively wide range. Here we made an assumption that the ratio  $M_{*,10}/F$  depend neither on  $M_{*,10}$  nor on  $F$ , meaning that this quantity only describe one overall nature of quiescent galaxies at one given redshift. We then make narrow redshift bins, cal-

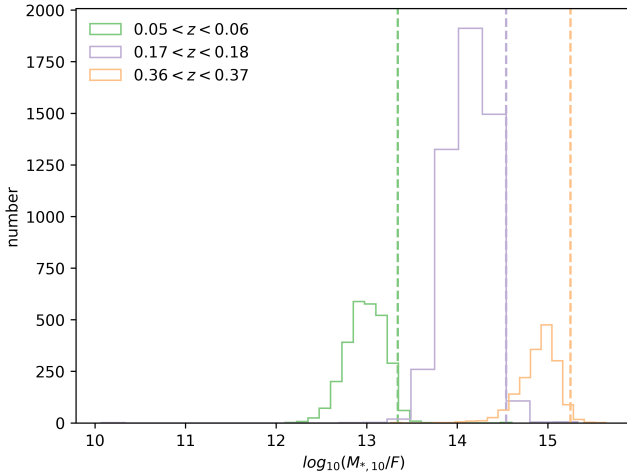


**Figure 2.** The distribution of  $M_{*,10}/F$  in three different narrow redshift bins. The vertical dashed line marks the 95% percentile distribution in each bin. Multiply this ratio by the flux corresponding to the r-band magnitude limit  $r_{crit} = 19.65$ , we then obtain the  $M_{*,10}$  limit at that redshift bin.

**Table 1.** Simulation parameters for different sets of simulation.

Set	$\xi$	$(M_h/M_*)_{\text{main}}$	$C_{\text{main}}$	$(r_s/R_{\text{eff}})_{\text{main}}$	$(M_h/M_*)_{\text{sat}}$	$C_{\text{sat}}$	$(r_s/R_{\text{eff}})$
D	1.0, 0.5, 0.2	49	8.0	11.6	49	8.0	11.6
D1	0.5	49	5.0	11.6	49	5.0	11.6
D2	0.5	49	8.0	6.0	49	8.0	6.0
D3	0.2	49	8.0	11.6	35	8.5	8.8
D4	0.2	49	8.0	11.6	75	8.0	15.0

culate the mean and standard deviation of the mass-to-flux ratio  $M_{*,10}/F$  and use Gaussian distribution to estimate the critical value  $M_{*,10}/F|_{crit}$ , where the cumulative probability reach 95%. Multiplying  $M_{*,10}/F|_{crit}$  by the corresponding flux of  $r_{crit}$ , we obtained the  $M_{*,10}$  limit at that redshift bin.

Fig 2 illustrate the procedure, it shows the dsitribution of  $M_{*,10}/F$  in three different redshift bins, with dashed line shows the 95% percentile of each bin. Operate this procedure iterative in each redshift bin and exclude galaxies whose  $M_{*,10}$  is lower than the limit, we obtained a sample with 95% completeness in  $M_{*,10}$  and is shown in Fig 3

## 2.4 Simulation

In order to build a intuitive understanding of the growth in  $M_{*,10}$  and  $\Gamma_{*,10}$  due to mergers, we utilize a collection of 8 sets dissipationless binary-merger simulations which has been used in Sonnenfeld et al. (2014) to construct a dry-merger model. These 8 sets of simulations has five different parameter settings and is reported in Table 1. Each set contains two simulations with nearly identical parameter settings except for their different orbital angular momentum in order to take both 'head-on' and 'off-axis' encounter into consideration. All orbits are parabolic.

The two progenitors, i.e. main galaxy and satllite galaxy , in each set of simulation are spherical symmetric and are composed of dark matter halo and stellar component. The stellar profile can be decribed by  $\gamma$  model (Dehnen (1993); Tremaine et al. (1994))

$$\rho_*(r) = \frac{3-\gamma}{4\pi} \frac{M_* r_*}{r^\gamma (r + r_*)^{4-\gamma}} \quad (10)$$

where  $M_*$  is the total stellar mass. The simulation adopt  $\gamma = 1.5$ .

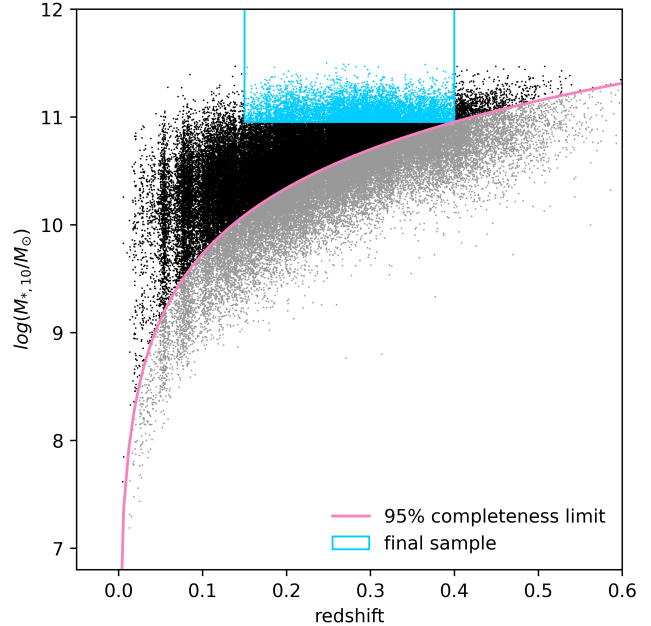


**Figure 3.** 95% completeness  $M_{*,10}$  limit as a function of redshift of our ETG sample, shown in pink solid line. Galaxies above this pink line is adopted in our sample, shown in black dots, and the grey dots that lies below are those being excluded

The dark matter halo is described by NFW profile (Navarro et al. (1996))

$$\rho_{DM}(r) = \frac{M_{DM,0}}{r(r+r_s)^2} \exp \left[ -\left( \frac{r}{r_{vir}} \right)^2 \right] \quad (11)$$

According to Nipoti et al. (2009),  $r_s$  is the scale radius, while  $M_{DM,0}$  is a reference mass. A exponential cut-off is adopted as a truncation of the halo, hence the total dark mass would not extend to infinity. As the summation of the two components, the total mass profile  $\rho(r) = \rho_*(r) + \rho_{DM}(r)$  is nearly isothermal: the slope  $\gamma'$  of the toal mass profile in 8 sets of simulation lies in the range of  $1.97 \sim 2.03$ .

The simulation is run with FVFP code (Fortran Version of Fast Poisson Solver, Londrillo et al. (2003); Nipoti et al. (2003)). The following code parameter values are adopted: minimum value of the opening parameter  $\theta_{min} = 0.5$  while the softening parameter  $\epsilon = 0.04R_{\text{eff}}$ , here  $R_{\text{eff}}$  represent the effective radius of the main galaxy. The timestep  $\Delta t$  is the same for all particles, while is allowed to vary depending on the maximum particle density  $\rho_{max}$  at that epoch. In particular, the timestep can be adapted by  $\Delta t = 0.3/(4\pi G \rho_{max})^{1/2}$ . The realisation of the initial condition is identical to that in Nipoti et al. (2009), with the mass of dark matter parts twice as heavy as stellar particles.

## 3 RESULT

### 3.1 The growth of $M_{*,10}$ and $\Gamma_{*,10}$ in simulation

In order to investigate the growth of these two parameters, we only need to focus on two snapshots of the simulation. The first snapshot is the initial state which contains the initial main galaxy and satellite galaxy, in fact, we only care about the main galaxy. The second snapshot is the final state when the merging process is finished leaving

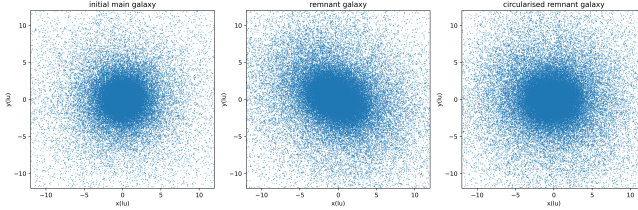


**Figure 4.** In this plot I choose the simulation set D3 to illustrate the mock images of main and remnant galaxies. The left panel shows the initial main galaxy, while the middle and right panels are the uncircularised and circularised remnant galaxy respectively. The unit is in code unit, instead of physical unit

a remnant galaxy. The word 'finish' means that the remnant stellar system is relaxed and virialised, while the remnant galaxy is the collection of dark matter particles and stellar particles that are bounded. We project the initial and remnant galaxies onto x-y plane so as to generate a mock observational image of these two, the mock image is shown in Fig. 4. The initial main galaxy is spherical, thus its image is a circle. In contrast, the remnant galaxy does not have this symmetry, hence we can observe that its image is an ellipse. In order to make a fair comparison, we then circularised the remnant ellipse. In particular, we measured the quadruple moment of the remnant galaxy image, and then stretch and rotate the image according to this quadruple moment until the image becomes a circle. Having done this circularisation, we are enabled to measure the  $M_{*,10}$  and  $\Gamma_{*,10}$  of both circularised initial main galaxy and circularised remnant galaxy, and make direct comparison to see how these two quantities grow during the merging process.

Actually, the mass, length, time and velocity are not in physical unit, but in code unit. That means we have the freedom to 'rescale' the simulation data, i.e. specify a physical value for these 'code unit', to generate galaxies with different size and mass. Traditionally, changing the mass and length unit may affect the timestep used in the simulation, but as we only focus on two snapshots and ignoring the time that one merger event takes, we believe this 'rescale' operation would not severely affect our result. The default scale of the simulation set the length unit to  $1\text{ kpc}$  and the total stellar mass of the main galaxy is  $\log_{10}(M_*) = 10.5$  so that the effective radius of which is  $R_e = 1.22\text{ kpc}$ . We then make two other modifications to make the initial main galaxy has  $R_e = 5, 10\text{ kpc}$ , meaning that the physical value of one code length unit is  $4.1, 8.2\text{ kpc}$  respectively in each modification. Therefore, for each set of simulations, we have three pairs of main and remnant galaxies. We then measured the  $M_{*,10}$  and  $\Gamma_{*,10}$  of all six galaxies in one set for all sets of simulations. The result is shown in Fig. 5.

We can easily observe that for all three merger ratios, the parameter  $\Gamma_{*,10}$  always shows a decreasing trend, while for larger, more massive galaxies, the decrease in  $\Gamma_{*,10}$  tends to be more significant. On the other hand, the growth of parameter  $\log M_{*,10}$  is a bit more complicated. In general, the growth in  $\log M_{*,10}$  is always less than the growth in the total stellar mass  $\log M_*$ , which may indicate that larger fraction of accreted mass are sunk in the outer region of the galaxy. In contrast with the  $\Gamma_{*,10}$ , smaller galaxies show a larger increase in  $\log M_{*,10}$ . Interestingly, if one pays more attention to the first two panels (top and middle panel), one can find that in some cases, the growth in  $\log M_{*,10}$  could be even negative after the merger. While for the largest merger ratio  $\xi = 1.0$  (bottom panel), the growth in  $\log M_{*,10}$  is always positive. The negative value informs us that the merger does not vary the entire density profile of the galaxy, and

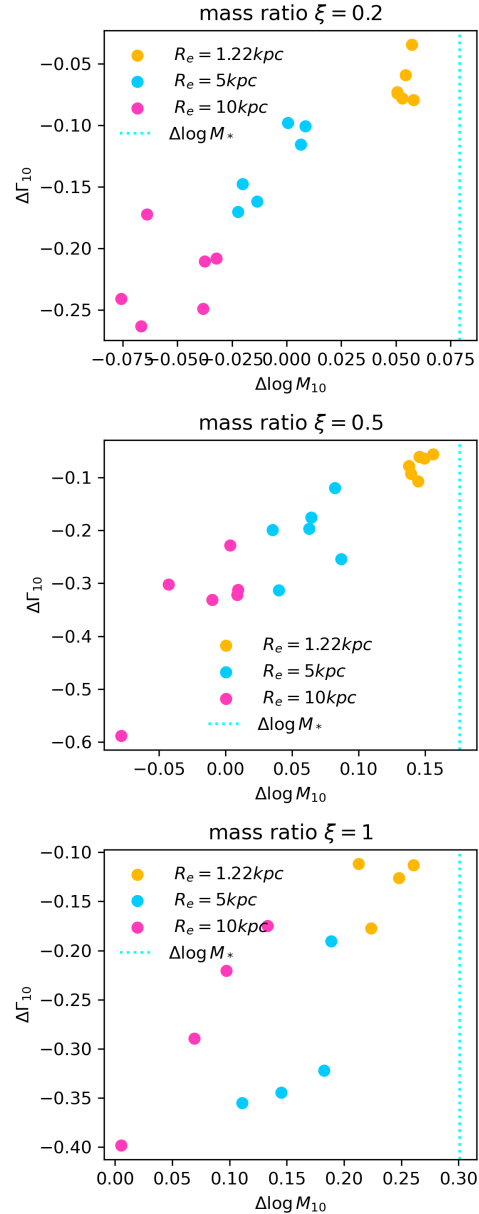


**Figure 5.** Three panels show the change in  $\log M_{*,10}$  and  $\Gamma_{*,10}$  due to mergers with three different merger ratio  $\xi$ , while the three colors represent different initial effective radius  $R_e$  of the main galaxy. The vertical dotted cyan line shows the logarithmic change in the total stellar mass for each merger ratio.

the inner region of galaxies may experience the most significant change comparing with the outer region. The impact on the inner region of galaxies tends to be stronger for mergers with smaller mass ratio. Small mass ratio minor-mergers may flatten the density profile, puffing-up the galaxies hence make  $\log M_{*,10}$  decrease and  $\log M_*$  increase simultaneously.

### 3.2 Observation result

Having investigated the result in simulations, we then operate the measurement to our observation sample. In fact, we have done a small modification on the total stellar mass. In case that we use the stellar mass measured by GAMA survey and use Sérsic parameter measured

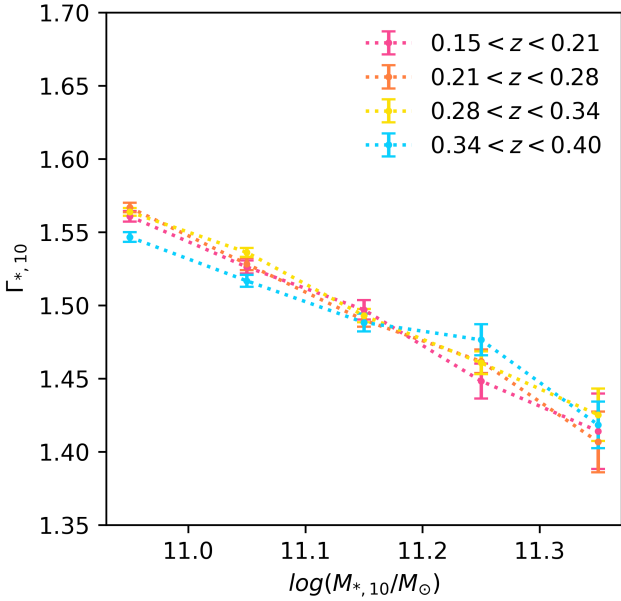


**Figure 6.** The  $M_{*,10} - \Gamma_{*,10}$  relation of our observation sample. The sample are divided into four redshift bins, and are shown in different colors. The error bar represents the standard error in each bins.

by KiDs survey, the flux of one single galaxy that has been used in the measurement of these two surveys may not be consistent. Here we made the assumption that the mass-to-flux ratio is a constant value in one single galaxy and calculated this ratio  $\Upsilon$  for each galaxy, using the data of total flux (converted from apparent magnitude) and stellar mass in GAMA survey. We then multiplied this ratio by the total flux measured by KiDs survey and obtained the stellar mass that is in consistent with the KiDs Sérsic parameter.

As a consequence of the completeness cut, galaxies with lower  $M_{*,10}$  value at higher redshift would be absent in our sample. To investigate the evolution trend in  $M_{*,10} - \Gamma_{*,10}$  relation, we have to either narrow the redshift range to include more low- $M_{*,10}$  galaxies or narrow the  $M_{*,10}$  range to include more high-redshift galaxies. In this work, we choose the latter one, meaning that we only focus on massive quiescent galaxies whose  $M_{*,10} \geq 10^{10.9} M_\odot$ . In addition, we set a lower limit on the redshift range  $z \geq 0.15$ . It's easy to observe some vertical stripe-like feature in Fig.3 at low redshift end, and is thought to be the effect of large scale structure by Driver et al. (2022). It is reasonable as the comoving volume at low redshift is relatively smaller, so it is more likely to suffer from cosmic variance. We thus determined this low-redshift cut in order to avoid such cosmic variance. The final sample we used to investigate the evolution is show by cyan dots in Fig.3. We binned the sample in redshift and  $M_{*,10}$ , then calculated the median value of  $\Gamma_{*,10}$  in each bin. The  $\Gamma_{*,10}$  result is shown as a function of  $M_{*,10}$  in Fig.6 and as a function of redshift in Fig.7.

In Fig.6, we could observe a anti-correlation between  $M_{*,10}$  and  $\Gamma_{*,10}$ . Comparing the data in four redshift bins simultaneously, we can hardly see the evolution trend in this relation. In addition, if we focus on  $\Gamma_{*,10}$  only, as shown in Fig.7, we could reach a similar conclusion that there is no significant evolution in  $\Gamma_{*,10}$ . The  $\Gamma_{*,10}$  value in five different  $M_{*,10}$  are all almost constant as the redshift grows. The error bars in these two plots are standard error in each bin, i.e the standard deviation divided by the square root of the number of

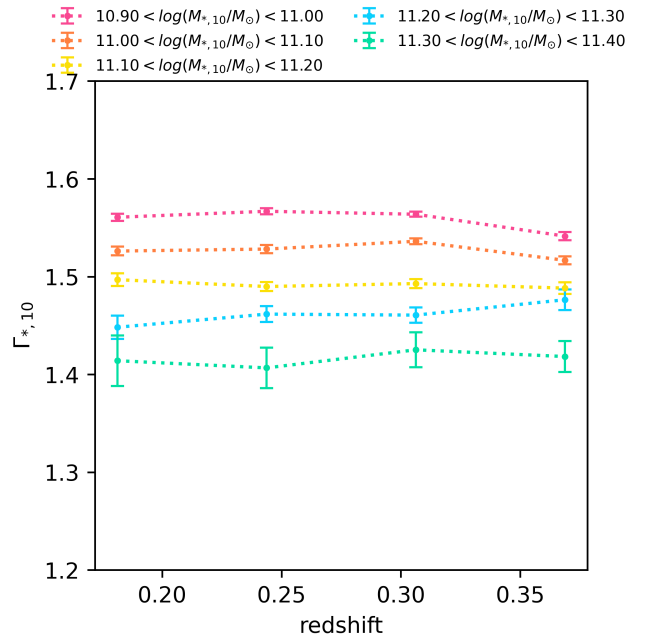


**Figure 7.**  $\Gamma_{*,10}$  as a function of redshift in each  $M_{*,10}$  bin. The sample are divided into five different  $M_{*,10}$  bins. The error bar represents the standard error in each bins.

galaxies in each bins. The error bar is relatively larger at higher  $M_{*,10}$  end, but it does not affect our conclusion as in Fig 6, the data points are still overlapping with each other in the same  $M_{*,10}$  bin and the  $\Gamma_{*,10} - z$  relation can still be reckoned as a horizontal line.

## REFERENCES

- Amaro V., et al., 2021, in Zelinka I., Brescia M., Baron D., eds, , Vol. 39, Intelligent Astrophysics, pp 245–264, doi:10.1007/978-3-030-65867-0\_11
- Baldry I. K., et al., 2010, *MNRAS*, **404**, 86
- Belli S., Newman A. B., Ellis R. S., 2015, *ApJ*, **799**, 206
- Bellstedt S., et al., 2020, *MNRAS*, **496**, 3235
- Bruzual G., Charlot S., 2003, *MNRAS*, **344**, 1000
- Calzetti D., Armus L., Bohlin R. C., Kinney A. L., Koornneef J., Storchi-Bergmann T., 2000, *ApJ*, **533**, 682
- Carollo C. M., et al., 2013, *ApJ*, **773**, 112
- Chabrier G., 2003, *PASP*, **115**, 763
- D'Eugenio F., et al., 2023, Evolution in the Orbital Structure of Quiescent Galaxies from MAGPI, LEGA-C and SAMI Surveys: Direct Evidence for Merger-Driven Growth over the Last 7 Gy (arxiv:2303.05520)
- Daddi E., et al., 2005, *ApJ*, **626**, 680
- Damjanov I., Zahid H. J., Geller M. J., Utsumi Y., Sohn J., Souchereau H., 2019, *ApJ*, **872**, 91
- Dehnen W., 1993, *MNRAS*, **265**, 250
- Dekel A., Burkert A., 2014, *MNRAS*, **438**, 1870
- Dokkum P. G. v., Franx M., 1996, *MNRAS*, **281**, 985
- Driver S. P., et al., 2022, *MNRAS*, **513**, 439
- Fagioli M., Carollo C. M., Renzini A., Lilly S. J., Onodera M., Tacchella S., 2016, *ApJ*, **831**, 173
- Fan L., Lapi A., De Zotti G., Danese L., 2008, *ApJ*, **689**, L101
- Gordon Y. A., et al., 2017, *MNRAS*, **465**, 2671
- Hamadouche M. L., et al., 2022, *MNRAS*, **512**, 1262
- Hilz M., Naab T., Ostriker J. P., 2013, *MNRAS*, **429**, 2924
- Hopkins P. F., Bundy K., Hernquist L., Wuyts S., Cox T. J., 2010, *MNRAS*, **401**, 1099
- Hopkins A. M., et al., 2013, *MNRAS*, **430**, 2047
- Kuijken K., et al., 2019, *A&A*, **625**, A2
- Li R., Napolitano N. R., Roy N., Tortora C., La Barbera F., Sonnenfeld A., Qiu C., Liu S., 2022, *ApJ*, **929**, 152
- Londrillo P., Nipoti C., Ciotti L., 2003, *Memorie della Societa Astronomica Italiana Supplementi*, **1**, 18
- Naab T., Johansson P. H., Ostriker J. P., 2009, *ApJ*, **699**, L178
- Navarro J. F., Frenk C. S., White S. D. M., 1996, *ApJ*, **462**, 563
- Newman A. B., Ellis R. S., Bundy K., Treu T., 2012, *ApJ*, **746**, 162
- Nipoti C., Londrillo P., Ciotti L., 2003, *MNRAS*, **342**, 501
- Nipoti C., Treu T., Bolton A. S., 2009, *ApJ*, **703**, 1531
- Oser L., Naab T., Ostriker J. P., Johansson P. H., 2011, *ApJ*, **744**, 63
- Roy N., et al., 2018, *MNRAS*, **480**, 1057
- Sonnenfeld A., 2020, *A&A*, **641**, A143
- Sonnenfeld A., Nipoti C., Treu T., 2014, *ApJ*, **786**, 89
- Tal T., van Dokkum P. G., 2011, *ApJ*, **731**, 89
- Taylor E. N., et al., 2011, *MNRAS*, **418**, 1587
- Toft S., et al., 2007, *ApJ*, **671**, 285
- Tremaine S., Richstone D. O., Byun Y.-I., Dressler A., Faber S. M., Grillmair C., Kormendy J., Lauer T. R., 1994, *AJ*, **107**, 634
- Trujillo I., et al., 2006, *MNRAS*, **373**, L36
- Trujillo I., Conselice C. J., Bundy K., Cooper M. C., Eisenhardt P., Ellis R. S., 2007, *MNRAS*, **382**, 109
- van Dokkum P. G., Brammer G., 2010, *ApJ*, **718**, L73
- van Dokkum P. G., Franx M., 2001, *ApJ*, **553**, 90
- van Dokkum P. G., et al., 2008, *ApJ*, **677**, L5
- van Dokkum P. G., et al., 2010, *ApJ*, **709**, 1018
- van der Wel A., et al., 2014, *ApJ*, **788**, 28

This paper has been typeset from a Te<sub>X</sub>/La<sub>T</sub>E<sub>X</sub> file prepared by the author.